PCCP

Computational investigations of Dienes defect- and vacancy-induced changes to electronic and vibrational properties of carbon fiber structural units

Journal:	*Physical Chemistry Chemical Physics*
Manuscript ID	CP-ART-08-2021-003930.R1
Article Type:	Paper
Date Submitted by the Author:	10-Nov-2021
Complete List of Authors:	Isbill, Sara; Oak Ridge National Laboratory, Shields, Ashley; Oak Ridge National Laboratory Kapsimalis, Roger; Oak Ridge National Laboratory Niedziela, Jennifer; Oak Ridge National Laboratory

Journal Name

ARTICLE TYPE

Cite this: DOI: 00.0000/xxxxxxxxxx

Computational investigations of Dienes defect- and vacancy-induced changes to electronic and vibrational properties of carbon fiber structural units†

Sara B. Isbill,* Ashley E. Shields, Roger J. Kapsimalis, and J. L. Niedziela

Received Date
Accepted Date

DOI: 00.0000/xxxxxxxxxx

Carbon fiber (CF) is a promising lightweight alternative to steel of significant interest for energy applications. As CF continues to find new uses and is exposed to new external conditions, a noninvasive method of monitoring its structural integrity is critical. Raman spectroscopy is a commonly used method for this monitoring; however, it is highly inferential and interpretation of the data is not always straightforward. In this work, we perform density functional theory (DFT) calculations to investigate changes in the vibrational properties of CF structural units (i.e., graphene and graphite) caused by monovacancy and Dienes defects as a foundation for modeling more complex defects that move our model toward that of realistic CF. Using large computational supercells, we are able to understand how these defects change the electronic structure and vibrational properties of graphene and graphite for interdefect distances near that of the lower experimental limit. The monovacancy opens an electronic bandgap at the K point. Although no such electronic gap is opened by the Dienes defect, both defects introduce flat defect bands near the Fermi energy. The Dienes defect creates long-range deviations to the phonons, leading to substantial broadening of the highest frequency optical modes in the band structure compared to that of the pristine material. In contrast, the phonon changes caused by the monovacancy are short range, and only minor changes to the band structure or phonon density of states were observed. These findings can assist in the interpretation of experimental results by providing atomic-scale insight into key electronic and vibrational features.

1 Introduction

Carbon fiber (CF) has gained much attention over the last several decades due to its high strength-to-weight ratio, which has made it a promising alternative to traditional materials in several energy-related industries. For example, CF used in place of steel in the automotive and aeronautical industries can reduce the overall vehicle weight, thereby increasing fuel efficiency.[1–3] CF can also be used to make longer wind turbine blades at the same weight, allowing increased wind-energy capture. Owing to their use in consumer products, understanding the complex relationship between the CF microstructure and overall material strength, which varies widely based on processing conditions, is important.[4,5] Although defects are generally believed to reduce the strength of CF by disrupting the graphitic network, some studies report increased strength and modulus of graphitic materials.[6,7] Raman spectroscopy noninvasively probes the long-range vibrational interactions (phonons) and can provide inferential information about the graphitic microstructure by monitoring changes to the peak shapes and locations, and it has been used extensively to investigate the relationship between spectral observables and thermomechanical properties.[8–13]

Despite the extensive efforts and progress made in interpreting the Raman spectra, a complete understanding of the experimental data is not yet available. In particular, it is known that pristine graphitic materials have only one first-order Raman-active mode leading to the formation of the G peak, and defects cause additional bands to be observed, called the D and D' peaks. Exactly how many peaks are present in these bands is unclear, as the number of peaks reported in the literature are strongly dependent on the fitting procedure used.[11,12,14–16] This spectral uncertainty leaves open interpretation for the fundamental physics

Nuclear Nonproliferation Division, Oak Ridge National Laboratory, Oak Ridge, Tennessee, 37830, USA; E-mail: isbillsb@ornl.gov

† Electronic Supplementary Information (ESI) available: See DOI: 00.0000/00000000.

at play, such as additional electron–phonon coupling routes and avoided band crossings. Computational studies of CF lattice dynamics where the atomic structure is precisely known can clarify the number of Raman-active modes and subsequently the expected number of peaks, providing new insights into appropriate fitting procedures and interpretation of the experimental spectra.

Owing to their structural complexity, most quantum-mechanical atomistic models use graphene and graphite as CF surrogates because they are present in the fiber microstructre. This is a reasonable initial approximation because the extent of graphitization has been shown to correlate with fiber strength.[17] A vast amount of literature exists that computationally investigates defects in graphitic materials,[18–21] and many of these studies focus on the Dienes (pentagon-heptagon pairs formed via a 90° bond rotation) and vacancy defects (Fig. 1).[19,22–27] However, these studies are often restricted to electronic properties, such as formation energies,[19,22,24,25,28,29] activation barriers,[19,23,26,30–35] and electronic band structures.[22,24,25,27,31,36–42] Far fewer studies systematically investigate changes to the lattice dynamics of graphene and graphite induced by defects, which can directly aid in the interpretation of Raman spectral studies of carbonaceous systems, and in the case of CF, potentially highlight manufacturing or operations issues. Although phonon frequencies have been reported for Dienes defects and vacancies, these results are restricted to the Γ point and are highly dependent on system size.[22,25,27,43–46] To our knowledge, only a few studies report the defect-induced changes to the phonon band structure and density of states (DOS).[25,27,47–49] These quantities are essential for comparison to experimental observables from inelastic neutron scattering and other vibrational spectroscopies and interpreting thermomechanical behaviors.

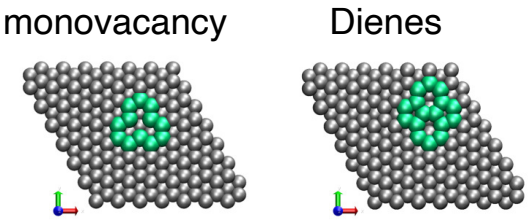

Fig. 1 Structures of monovacancy (left) and Dienes (right) defects in 7 × 7 hexagonal graphite cell. Atoms of defect are shown in green.

To investigate the alteration on the phonon band structures induced by experimentally relevant defect densities, supercells are needed that can support interdefect distances approaching 20 Å.[9] For graphene, this is a 120-atom hexagonal graphene layer. To understand how the spectral indicators may change as a result of the neighboring atomic layers, graphite cells are needed that further increase the number of atoms. Thus, these calculations can quickly become intractable without highly parallel computing architectures and software that can maximize computational efficiency. Real-Space Multigrid (RMG) DFT[50,51] is an electronic structure theory package that represents wave functions, electron charge density, potentials, and the Kohn–Sham Hamiltonian on a real—rather than reciprocal—space grid of points. This reduces the number of fast Fourier transforms needed during the calculation and allows electron charge density, potential, and wave function be distributed by region over the processors, which improves efficiency on highly parallel computer architectures. RMG has been used to calculate the vibrational properties of several materials in excellent agreement with other DFT software and experiments.[52]

This work investigates the changes induced in a variety of electronic and vibrational properties with the inclusion of a Dienes defect and a monovacancy in graphene and graphite using DFT. After a review of the computational methods (Section 2), the defect-induced changes to several electronic and vibrational properties are discussed (Section 3).

2 Computational Methods

Using DFT as implemented in RMG, we calculated the non–spin polarized minimum-energy structure and formation energy of monovacancy and Dienes defects in graphene and graphite. We investigated changes in formation energy for hexagonal supercells composed of 7 × 7, 8 × 8, and 10 × 10 unit cells in the *a* and *b* directions, with cell dimensions of 17.3 × 17.3 Å, 19.7 × 19.7 Å, and 24.7 × 24.7 Å, respectively. The supercell dimension in the *c* direction was 13.9 Å in all graphite cells, corresponding to four planar carbon layers in the AB-stacked graphite structure. A single carbon layer with 13.9 Å of vacuum was used to model monolayer graphene. The van der Waals Density Functional (vdW–DF) exchange-correlation functional was used within the generalized gradient approximation to ensure correct description of the van der Waals interactions.[53] Owing to the supercell size, Brillouin zone (BZ) integration was restricted to the Γ-point for structural relaxation and phonon calculations, and a 3 × 3 × 3 mesh with a Gaussian smearing width of 0.1 eV was used to calculate more accurate occupations for the electronic band structure and electronic DOS. In the case of the 8 × 8 pristine graphene cell, symmetry was neglected in the electronic band structure calculations to obtain auto-generated k-points consistent with the other calculations which was necessary to obtain the correct electronic DOS. Core electrons were described using an ultrasoft pseudopotential.[54] Methfessel and Paxton's method, with a smearing width of 0.1 eV, was used to describe the orbital occupation.[55] Structures were optimized until all forces were less than 0.03 eV/Å. DFT parameters for the phonon calculations were the same as those used for the optimizations. Additional parameters, including those specific to RMG, can be found in Table 1 in the Electronic Supplemental Information (ESI†).

The smallest supercell with convergence of both formation energy and key bond lengths around the defect was used to calculate phonons via the finite displacement method[56] as implemented in Phonopy[57] using RMG as the DFT engine.[52] Displacements for graphene and graphite were automatically generated in Phonopy, with an adjusted symmetry tolerance of 1×10^{-5} Å and 1×10^{-2} Å, respectively, which were needed to accurately describe the highest-energy optical modes in graphene and interlayer shearing in graphite (ESI†, Figs. 1 and 2). These symmetry tolerances were prohibitively expensive for the low-symmetry defect systems; however, the number of displacements required to

calculate the force constants with a symmetry tolerance of 0.1 Å was sufficient to describe the high-energy optical modes and interlayer shearing in the defective modes and has been used for the defect systems in this work. A symmetry tolerance of 0.1 Å was also used for the sumo seeK-path module[58–60] to determine the k-path and location of high-symmetry point in the BZ for the same reason (ESI†, Fig. 3). Although supercells were needed to achieve the desired defect density and are also required to achieve accurate phonons using the finite displacement method, their use leads to artificial folding of phonon band structures due to the reduced size of the supercell BZ compared to that of a unit cell.[61,62] To account for this, the phonon band structure was unfolded according to the method of Ikeda et al. as implemented in the UPHO package.[62] Phonon DOS calculations were performed in Phonopy using a mesh of 24 × 24 × 20 with a Gaussian smearing of 4 meV (33 cm^{-1}) for all cases unless otherwise stated.

3 Results and Discussion

3.1 Monovacancy

Monovacancy defects are formed by removing a single atom from the lattice (Fig. 1). In the following sections we will discuss the formation energy and structure of the relaxed monovacancy defect (Section 3.1.1), electronic structure (Section 3.1.2), and vibrational properties (Sections 3.1.3 and 3.1.4). We also compare each calculated property to the pristine system to understand the changes induced by the defect.

3.1.1 Formation energies and relaxed structures

The formation energy of a monovacancy defect in graphene and graphite was calculated as shown in Equation 1, where d and p denote the defect and pristine systems, respectively, and n is the number of atoms in the respective supercell. To ensure minimal interaction between defects and their periodic images, the formation energy was calculated for a single defect in three different sized monolayer graphene and AB-stacked four-layer graphite supercells: 7 × 7, 8 × 8, and 10 × 10. The absolute formation energies are given in Fig. 2.

$$E_{form} = E_d - \frac{n_d}{n_p} E_p \quad (1)$$

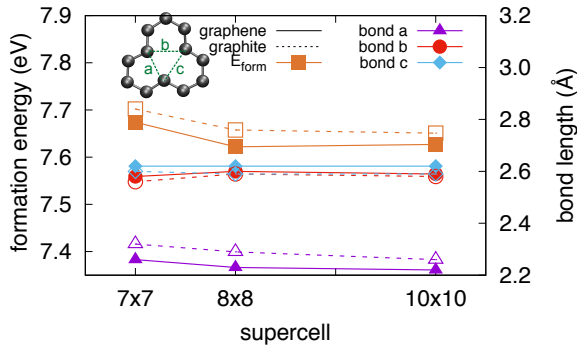

Fig. 2 Formation energies and key bond lengths of the relaxed monovacancy defect in graphene (closed symbols, solid lines) and graphite (open symbols, dashed lines).

As shown in Fig. 2, the formation energy of the monovacancy is similar across all cell sizes, with E_{form} 0.05 eV greater for an interdefect distance of 17 Å (7 × 7) compared to 24 Å (10 × 10). E_{form} is also larger by 0.02–0.03 eV for the monovacancy defect in graphite than graphene. For vacancy creation in each cell size for each system, three dangling bonds result. During geometry optimization, the symmetry is broken as two of the dangling bonds move closer to one another and form a bond, leaving only one dangling bond in the structure which moves out of plane by 0.4 Å in graphene but only 0.2 Å in graphite. This reduced out-of-plane displacement likely results from weak van der Waals interactions between neighboring layers in graphite, which is absent in graphene. The relaxed bond lengths around the vacancy are given in Fig. 2. The formation energies and structural changes associated with the Jahn–Teller distortion calculated here are in agreement with previous non–spin polarized studies,[28,63] although those that include spin polarization report less out-of-plane displacement.[37,64]

Because of the computational cost associated with such large supercell calculations, only a single system size was selected for further analysis, chosen based on defect interactions with periodic images, relaxed geometric structure, and computational efficiency. Based on these comparisons, high-level electronic band structures and phonon calculations were performed for the monovacancy in the 8 × 8 graphene cell and the four-layer 7 × 7 graphite cell, and all of the following discussion on the monovacancy defect focuses on these systems.

3.1.2 Electronic band structure

The electronic band structure along the Γ–K–M–Γ path and electronic DOS for energies near the Fermi energy (E_F) of pristine and monovacancy-defective graphene and graphite are shown in Fig. 3. The path along the Brillouin zone and an annotated version of the graphene panel of Fig. 3 which points out the key features in the following discussion are provided in the ESI† (Fig. 3 and 4). Pristine graphene and graphite are semimetals, with the valence and conduction bands meeting at the K point in the BZ, forming a Dirac point.[65,66] The origin of the D peak in the Raman spectrum of defected carbon materials is hypothesized to result from a complex electron–phonon coupling mechanism arising from this electronic anomaly.[67] A single monovacancy defect shifts E_F by −0.11 and −0.05 eV in graphene and graphite, respectively, and opens a bandgap of 0.32 eV in graphene, consistent with similar studies in the literature.[22,39] No such bandgap is seen in graphite, most likely because of the lower defect concentration in this material (0.25% in graphite compared to 1.02% in graphene) and defect shielding by the pristine layers. In both graphene and graphite, an energy band at ≈+0.2 eV relative to the monovacancy E_F is seen which is relatively flat across the electronic band structure path investigated here. The electronic DOS of both pristine graphene and graphite show a single, low-density peak at E_F that splits in the presence of an monovacancy defect, creating a peak just above E_F that corresponds to the flat band at +0.2 eV and the blueshift of the electronic bands at K which form the bandgap.

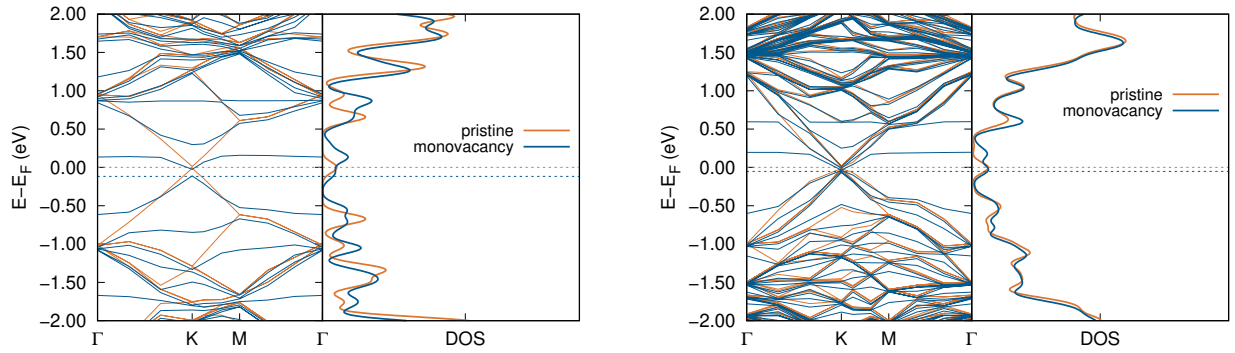

Fig. 3 Folded electronic band structure along the Γ–K–M–Γ path in the BZ and electronic DOS around E_F (dashed line) for the monovacancy defect in graphene (left) and graphite (right).

3.1.3 Phonon DOS

The phonon DOS for the pristine and monovacancy-defective systems were calculated to provide a qualitative understanding of how the phonons change in response to defects. The phonon DOS of the monovacancy defect in both graphene and graphite is shown in Fig. 4. Graphene experiences very minor changes in density of the lower frequency modes. Specifically, the density between 50 and 400 cm^{-1} is slightly larger for the defective system. At the Van Hove singulartiy (point in the phonon DOS where the derivative with respect to frequency is undefined) around 450 cm^{-1}, the densities of both the pristine and defective system are nearly equal. The monovacancy has higher density at the minimum in DOS near 530 cm^{-1}; however, the monovacancy has reduced density for the region from ∼650 to 800 cm^{-1}. Additionally, the monovacancy system has notably larger density from ∼1040 to 1350 cm^{-1}, but a minor reduction in density is seen for the Van Hove singularities at 1380 and 1500 cm^{-1} in the defective system. Monovacancy-defective graphite shows very little change compared to the phonon DOS of pristine graphite. A slight increase in density is seen near 1350 cm^{-1}, whereas slight decreases are seen at 800, 1380, and 1540 cm^{-1}.

These results are consistent with the work of Al-Qasir et al. who calculated the phonon DOS of graphite containing a divacancy defect and found the largest changes in phonon DOS above 1000 cm^{-1},[47] which is consistent with our findings for graphene. This is explained by comparing the defect density modeled between our two systems and that of Al-Qasir et al. Our systems each contain only a single monovacancy defect, but the total number of atoms is four-times larger in graphite. Thus, the density of defects in the graphene system is 1.0%, but it is only 0.25% in graphite. The defect density simulated by Al-Qasir et al. was 0.7%. This highlights that the onset of changes to the phonon DOS because of vacancies lies somewhere in the density range 0.2–0.7%. Below this value, vacancies will be undetectable by analyzing the phonon DOS because they will be essentially screened by the large number of phonons arising from the atoms away from the defect.

Though not detectable in the total phonon DOS of graphite, changes to the phonon DOS are present, and we can begin to understand these changes by looking at the contributions from

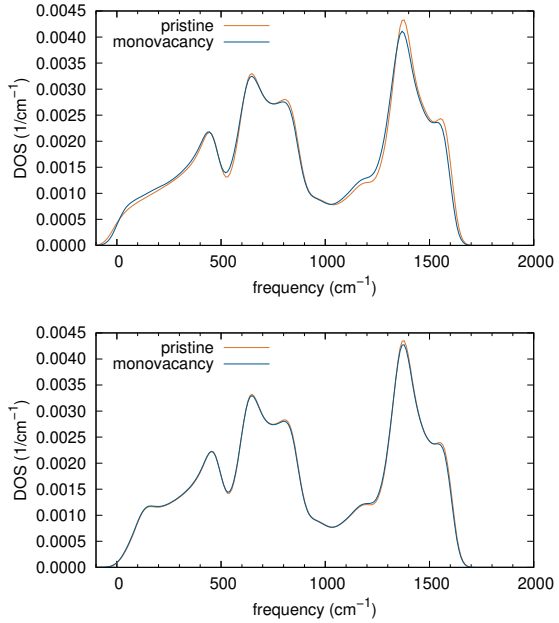

Fig. 4 Phonon DOS of monovacancy in graphene (above) and graphite (below).

atoms near the defect site by investigating the partial phonon DOS. The contributions to the phonon DOS of individual atoms near the monovacancy defect in graphene and graphite are shown in Fig. 5, where nn denotes nearest neighbor, and the partial phonon DOS plots are offset by 0.002 $1/cm^{-1}$. Contributions are shown for atoms up to 2.90 Å from the vacancy, corresponding to the seventh nearest neighbor, excluding atoms in the neighboring layers for graphite. Comparing the left and right panels, for the monovacancy defect in graphene and graphite, respectively, shows that the partial phonon DOS contributions are minimally influenced by the presence of the weakly interacting layers in graphite. The only deviation to this is seen for atoms 1 and 2 nn from the vacancy, where the atoms in graphite have larger contributions to the phonon DOS at very low frequency (less than 100 cm^{-1} for 1 nn and less than 200 cm^{-1} for 2 nn) for the corresponding atoms in graphene.

From Fig. 5, we see a large increase in density below 530 cm^{-1}

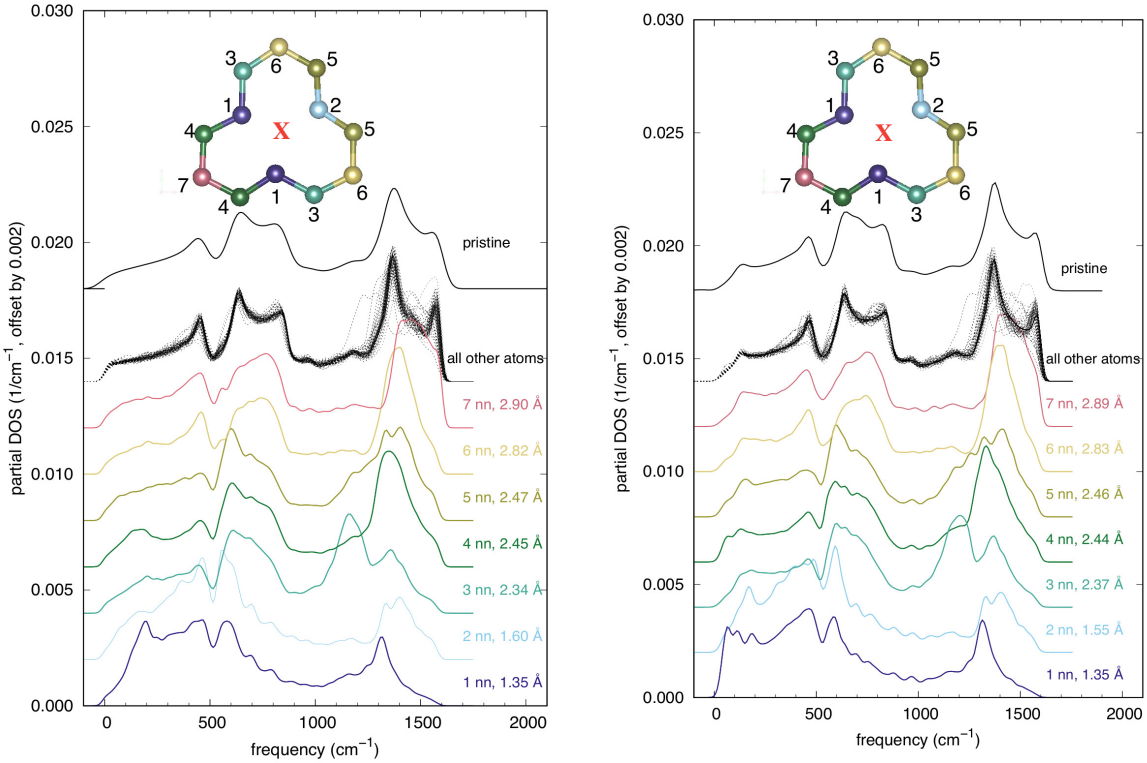

Fig. 5 Partial phonon DOS of atoms near the monovacancy defect in graphene (left) and graphite (right), where nn denotes nearest neighbor and the distances are given relative to the vacancy, denoted by the red "X". Atoms beyond 7 nn are plotted together (all other atoms), and the partial phonon DOS of an atom from the pristine material (pristine) is also shown. All phonon DOS plots are offset by 0.002 1/cm^{-1} for clarity. A 10 × 10 × 8 mesh was used to generate the projected DOS.

for 1 and 2 nn atoms. 2 nn has particularly large density for phonons in the region 400–600 cm^{-1}. Figures 5 and 6 in the ESI† reveal that the changes seen in the phonons of 1 and 2 nn atoms arise from an increase of both in-plane and out-of-plane contributions up to ∼450 cm^{-1}. Fig. 5 also shows large changes in the high frequency region up to 6 nn. This is not surprising since phonons near 900 cm^{-1} are related to in-plane vibrations and atoms 7 nn from the lattice vacancy are less than 3 Å away. However, the large decrease in phonon DOS for 1, 2, and 3 nn atoms, and the large increase in density for phonons near 1150 cm^{-1} is consistent with the decrease in phonon density above 1000 cm^{-1} seen in Fig. 4.

The shifts in density at higher frequencies are consistent with the in-plane structural changes associated with the Jahn–Teller distortion of the vacancy. For example, 1 nn atoms lose the 1.42 Å bond to the missing atom (1 nn–X), and a weaker 2.23 Å bond is formed between them (1 nn–1 nn). Additionally, one of the remaining C–C bonds contracts (1 nn–4 nn), but the other is elongated (1 nn–3 nn). Although the changes to these bond lengths are small (−0.022 and +0.017 Å for an overall deviation of −0.005 Å), a minor redshift in frequency is expected compared to the partial phonon DOS of an atom in a pristine material. Indeed, a very minor redshift is seen in the 1300–1500 cm^{-1} phonon DOS features for 1 nn in Fig. 5. Similar behavior is seen for 2, 4, and 5 nn and is consistent with both contraction and elongation of bonds containing these atoms. Consistent with the expansion of all three bonds containing 3 nn atoms (+0.064 Å), 3 nn shows a much more significant shift to lower frequencies. Shifts also generally decrease with distance from the defect as deviations away from the pristine C–C bond length are reduced.

3.1.4 Phonon band structure

In addition to investigating the number of states at a given frequency across the entire BZ, we can look at the phonon band structure for information about changes to the lattice dynamics at certain high-symmetry points and do so along the Γ–K–M–Γ k-path. While large system sizes provide more experimentally relevant interdefect distances, they also increase the complexity of the phonon band structure. As the real-space cell size increases, the reciprocal space cell gets smaller and the high-symmetry **q** points of the unit cell BZ and supercell BZ are no longer equivalent. This leads to bands that "fold" to fit into the reduced supercell BZ. Methods have been developed which use the translational symmetry of the underlying crystal structure to project the supercell eigenvectors onto those of the primitive cell, the deviations from which are accounted for by calculating the spectral weights. It is worth noting that the translational symmetries of pristine and defective cells are not completely equivalent; however, it is reasonable to consider low defect concentrations as a perturbation to the pristine system which is essentially what is done in the following sections.

Panels A-C of Figure 6 shows the phonon DOS, folded, and unfolded band structures for pristine (A) and monovacancy-defective (B) graphene where the colored legend with the un-

folded band structure denotes the spectral weighting. The unfolded band structure for pristine graphene is in qualitative agreement with the literature.[48,49] Figure 6C shows the spectral weight of modes at the Γ and K points for monovacancy-defective systems. Especially for graphene, a small amount of broadening is seen around the transverse and longitudinal optical (TO and LO, respectively) branches along the full path, and new spectral-weight maxima, denoted by the points in Fig. 6C, are seen across nearly the full frequency range at Γ and K, though the spectral weight of these new modes are generally very low. Similar changes near the K point were also calculated by Bouzerar et al. for a 5% defect concentration.[49] The distinct low spectral weight band around 0 cm^{-1} for the graphene monovacancy is the same artifact of the non–spin polarized calculation discussed previously.

The folded and unfolded band structure of pristine graphite is given in Fig. 6D. The weak interlayer shearing modes in graphite introduce new bands around 130 cm^{-1} at the Γ point which are absent in graphene. Despite the out-of-plane displacement of an atom through Jahn-Teller distortion of the vacancy, these modes are not changed in the defective system (Fig. 6E). In fact, there are only minor changes in the unfolded band structure between the pristine and monovacancy-defective graphite systems, as intuited from the phonon DOS results in Section 3.1.3.

Looking more closely at panels C and F of Figure 6, there are a few changes between the pristine and defective systems worth noting. Looking first at the Γ point, there is a small reduction in spectral weight of the degenerate bands near 1560 cm^{-1}. Additionally, the monovacancy defect induces a small redshift in frequency for the 1560 cm^{-1} mode of 11 and 5 cm^{-1} in the graphene and graphite systems, respectively. The frequency of these modes in both the pristine and defective systems is consistent with the *G* peak measured with Raman spectroscopy (∼1580 cm^{-1}).[68,69] Moving to the K point, there are notable reductions in the spectral weight of the modes at 1200, 1270, and 1460 cm^{-1}. Additionally, the mode near 1200 cm^{-1} shifts from 1203 to 1199 cm^{-1} in defective graphene. Two new modes with small but non-negligible spectral weight near 800 and 1460 cm^{-1} in monovacancy-defective graphene and 800 and 1500 cm^{-1} in monovacancy-defective graphite appear. Inspection of the defect eigenvectors reveals the mode at 800 cm^{-1} arises from an out-of-plane rocking mode of the C–C bonds which is damped at the defect while the mode at 1460 or 1500 cm^{-1} is related to the disruption of in-plane C–C asymmetric stretching modes. In graphite, the largest eigenvectors in these modes reside on atoms in the layer which contains the defect, and are generally at least an order of magnitude larger than eigenvectors on atoms in pristine layers.

3.2 Dienes defect

Dienes defects are formed through a 90° bond rotation which transforms four hexagons into a pair of heptagons and a pair of pentagons. In the following subsections we will discuss the formation energy and structure of the relaxed Dienes defect (Section 3.2.1), electronic structure (Section 3.2.2), and vibrational properties (Sections 3.2.3 and 3.2.4. We also compare each calculated property to the pristine system to understand the changes induced by the defect.

3.2.1 Formation energies and relaxed structures

The formation energy of Dienes defects in graphene and graphite was calculated as shown in Equation 1 for a single defect in 7 × 7, 8 × 8, and 10 × 10 supercells. The absolute formation energy and length of the rotated C–C bond in the relaxed structures is shown in Fig. 7.

The optimized structure of the Dienes defect was consistent across all cell sizes for graphene and graphite; however, the formation energy decreased almost linearly from 5.1 eV in the 7 × 7 cell to 4.9 eV in the 10 × 10 cell (Fig. 7), consistent with the work of Shirodkar and Waghmare (ESI†, Fig. 7).[25] When the C–C bond was rotated in-plane to form the 5–7 ring pairs, structural relaxation did not yield any out-of-plane displacements. The literature reports that the planar Dienes defect is a transition state between two structures with out-of-plane relaxations.[44,70] In one structure, the two atoms of the rotated C–C bond are displaced in the same out-of-plane direction, but they are displaced in opposite out-of-plane directions in the other. The planar graphene defect does contain two sizable imaginary modes (58i and 40i cm^{-1}) in which the eigenvectors on the defect atoms correspond to the two out-of-plane displacements. However, these imaginary modes are not seen for graphite, and manually breaking the planar symmetry of graphite led to out-of-plane displacements of only ∼0.04 Å, significantly less than the value reported by others.[44,70] This suggests that the van der Waals interaction between layers in graphite prevents out-of-plane relaxation of the Dienes defect. Because graphene and graphite were used as surrogates for CF where weak interactions between layers are very likely, phonons will be calculated for the planar defect in both graphene and graphite in the following discussion.

Because of the structural convergence for the Dienes defect in the 7 × 7 cell and literature reports that vibrational properties of Dienes defects are qualitatively converged for supercells of this size,[25] the 7 × 7 planar Dienes defect for both graphene and graphite is used for further analysis.

3.2.2 Electronic band structure

The electronic band structure and DOS for energies near E_F of pristine and Dienes-defective graphene and graphite are shown in Fig. 8. Unlike the monovacancy, the Dienes defect does not alter the Dirac cone at the K point in the electronic band structure, preserving the semimetallic nature of Dienes-defective graphene and graphite. Although there are no notable changes in the electronic band structure at the K point, the Dienes defect does introduce a relatively flat electronic band at ≈+0.5 eV above E_F at the Γ point. Additionally, E_F shifts by 0.02 and 0.004 eV for graphene and graphite, respectively. Due to the negligible change in the Dirac point for the Dienes defect, the electronic DOS near E_F is also unchanged, resulting in a single, low density peak at E_F, but a peak at 0.5 eV in graphene arises from the flat defect band at Γ.

Several studies confirm the formation of the flat electronic band

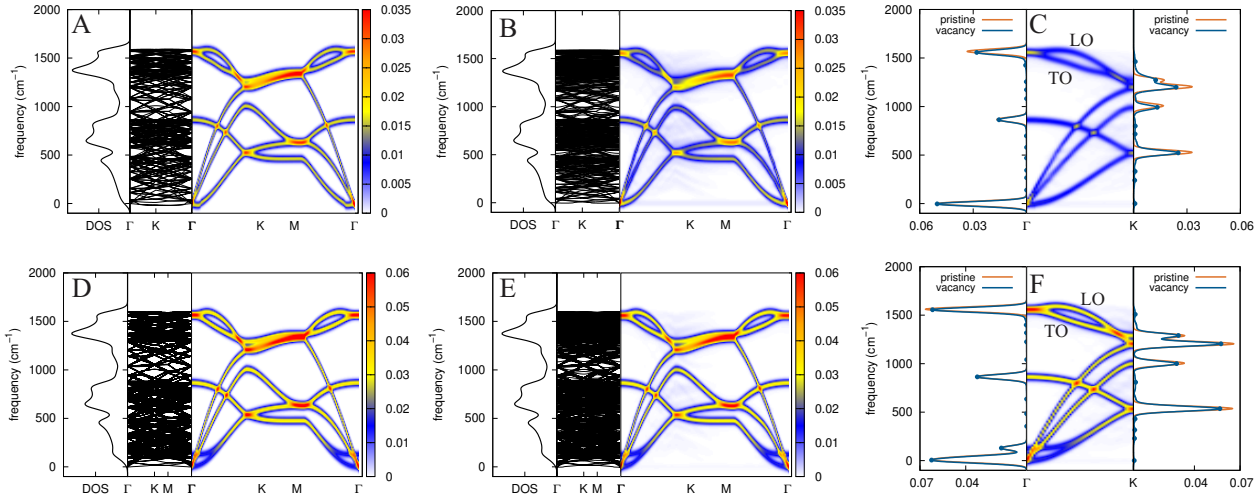

Fig. 6 Phonon DOS, folded, and unfolded band structures of pristine (A) and monovacancy-defective (B) graphene and pristine (D) and monovacancy-defective (E) graphite. (C) and (F) shows line cuts of the spectral weight at the Γ and K points of monovacancy-defective graphene and graphite, respectively, where points denote maxima in the spectral weight of the defective system.

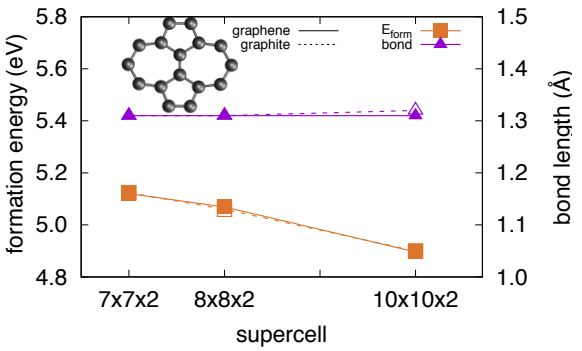

Fig. 7 Formation energies and key bond lengths of the relaxed Dienes defect in graphene (closed symbols, solid lines) and graphite (open symbols, dashed lines).

at 0.5 eV for Dienes-defective graphene.[25,27] These studies also report that a bandgap of nearly 0.2 eV opens in the presence of a Dienes defect[25,27]; however, Shirodkar and Waghmare explain that electronic band folding of graphene supercells can complicate interpretation in certain high-symmetry supercells.[25] For a 7×7 supercell, which was used in the present work, they do not calculate a bandgap at K,[25] consistent with our findings.

3.2.3 Phonon DOS

The phonon DOS of the Dienes defect in graphene, given in the top panel of Fig. 9, shows significant deviations from the phonon DOS of the pristine system, which is consistent with reports in the literature.[25] Starting from the low-frequency regime, the first notable feature is the increased density of imaginary states, shown as negative frequency modes in Fig. 9, compared to pristine graphene. This results from the choice to use the planar rather than buckled defect to better model a graphene-type sheet in CF as discussed in Section 3.2.1. Minor changes also occur in the density of the peaks around 450 and 530 cm^{-1}. Relative to the pristine case, for the Dienes defected case the DOS is reduced at 450 cm^{-1}, but it is increased at 530 cm^{-1}. The DOS peaks between 1360 and 1500 cm^{-1} are significantly broadened, removing the small dip between the two Van Hove singularities around 1200 cm^{-1} and increasing the highest-frequency phonons by approximately 40 cm^{-1}. Additionally, a low DOS peak around 1850 cm^{-1} is seen that corresponds to the stretching mode of the rotated C–C bond. The phonon DOS of Dienes-defective graphite shows significantly fewer changes. The broadening around 1300 and 1600 cm^{-1} is almost completely removed, with only a slight increase in density near 1200 and 1700 cm^{-1} and a reduction of DOS at the Van Hove singularity around 1400 cm^{-1}. The mode at 1850 cm^{-1} is visible, but low in density.

The partial phonon DOS for atoms near the Dienes defect in graphene and graphite are given in Fig. 10, where the distances are given from the center of the rotated C–C bond. Like the monovacancy, the partial phonon DOS is relatively unchanged between graphene and graphite, and the only differences occur at very low frequencies (less than 100 cm^{-1}). The most significant change to the total phonon DOS in Dienes-defective graphene is the broadening of the high-frequency peaks and the new peak at 1850 cm^{-1}. The latter clearly arises from the atoms nearest the defect (1 nn) and analysis of the phonon eigenvectors further reveals it is the symmetric stretching mode parallel to the rotated bond. The partial phonon DOS of the 1 nn atoms also reveals a small peak just above 1700 cm^{-1}. A larger peak at the same frequency for 3 nn atoms is seen. The eigenvectors for this mode shows the atoms of the rotated C–C bond symmetrically move perpendicular to the rotated C–C bond, but the 3 nn atoms move toward the defect with large displacements. This mode contributes significantly to the broadening of the right-hand side of the DOS plot. Atoms at 1, 2, 4, and 5 nn show a redshift in the DOS near 1500 cm^{-1}. Note, changes to the phonon DOS are seen for atoms well beyond 5 nn, as shown by the dispersion of peaks for "all other atoms" in Fig. 10, indicating that the influence of the Dienes defect is fairly long range.

Again, changes in the partial phonon DOS compared to the

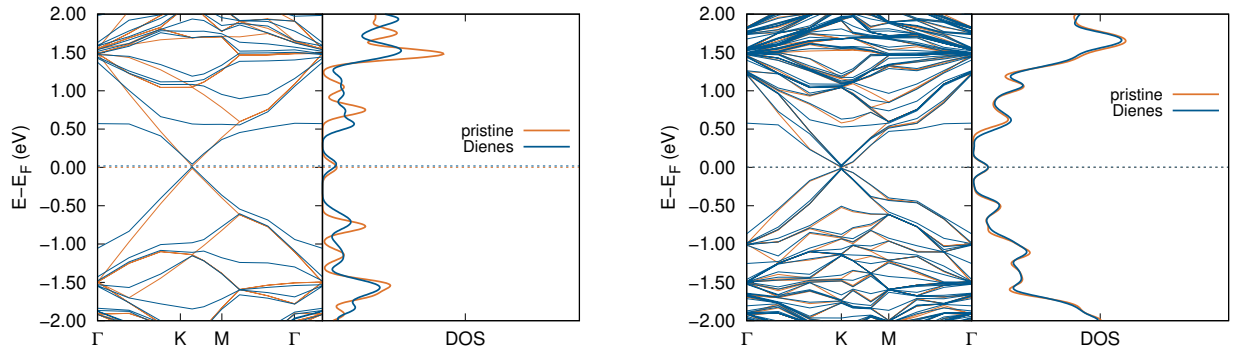

Fig. 8 Folded electronic band structure along the Γ–K–M–Γ path in the BZ and DOS around E_F (dashed line) for the Dienes defect in graphene (left) and graphite (right).

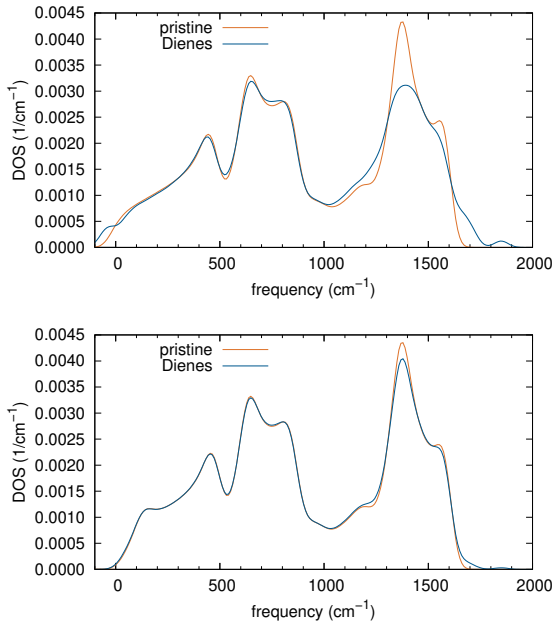

Fig. 9 Phonon DOS of Dienes in graphene (above) and graphite (below).

pristine material can be reconciled by an investigation into the structural changes associated with the defect. The 1 nn atoms contribute density ranging from 1100 to 1350 cm^{-1} and around 1850 cm^{-1}, as mentioned previously. Inspection of the bond lengths involving 1 nn atoms show two of the three bond lengths increase (1 nn–2 nn, +0.042 Å per bond), consistent with the redshift toward 1000 cm^{-1}. The third bond length, which is the rotated bond (1 nn–1 nn), significantly contracts (−0.111 Å), resulting in the high-frequency peak near 1850 cm^{-1}. A similar, though less severe, shift to lower frequencies is seen for 2 nn, where two bond lengths increased (2 nn–1 nn and 2 nn–3 nn) and the other decreased (2 nn–4 nn) for a total change of +0.025 Å. All three bonds containing 3 nn atoms decreased in length, leading to the notable redshifts in Fig. 10; contrariwise, all three bonds containing 4 and 5 nn atoms increased in length, leading to the blueshift in the partial phonon DOS in the higher frequency regime.

3.2.4 Phonon band structure

Figure 11 shows the phonon DOS, folded, and unfolded band structures for Dienes-defective graphene (A) and graphite (B). It is clear that the Dienes defect most significantly changes the high-frequency bands along the chosen path. In particular, the two highest frequency optical modes show significant broadening toward higher frequencies at both Γ and K in graphene (C) and graphite (D), consistent with the changes seen between 1300 and 1500 cm^{-1} in the partial phonon DOS (Fig. 10, left panel). Two low spectral weight bands around 1700 and 1850 cm^{-1} can be seen, which arise from the defect.

In Fig. 11D, the only notable change in frequency seen for graphite is a slight redshift and broadening of the mode around 1550 cm^{-1} at the Γ point, which is also seen in graphene. However, several additional differences are obvious between the pristine and Dienes-defective graphene band structures, particularly at K. There is a minor redshift of the mode near 1200 cm^{-1} that we also observed with the monovacancy defect. For the Dienes defect, the shift is 4 cm^{-1} in graphene and the peak location in graphite is unchanged. The pristine graphene mode at 1274 cm^{-1} is blueshifted by 8 cm^{-1} to 1282 cm^{-1}, broadening this peak toward higher energies. The same behavior is seen at the band near 1550 cm^{-1}. In pristine graphene, only one maxima in spectral weight is seen at this frequency because there are two degenerate bands. However, the spectral weight of this mode is significantly decreased in the Dienes-defective system and a new spectral-weight maxima is calculated at 1644 cm^{-1}.

3.3 Comparison of defects

Monovacancy and Dienes defects are some of the most studied defects in graphitic systems because of their reasonable formation energies and supposed prevalence. By calculating the electronic and vibrational properties of both defects using a consistent computational method and cell sizes, we can directly compare our results for both defect types.

The electronic structure changes are rather different between the two classes of defects investigated here. Although the monovacancy defect opened a sizable bandgap at K (0.32 eV), the Dirac cone for the Dienes defect was unchanged, even in graphene, which models a higher defect density. The shift in Fermi ener-

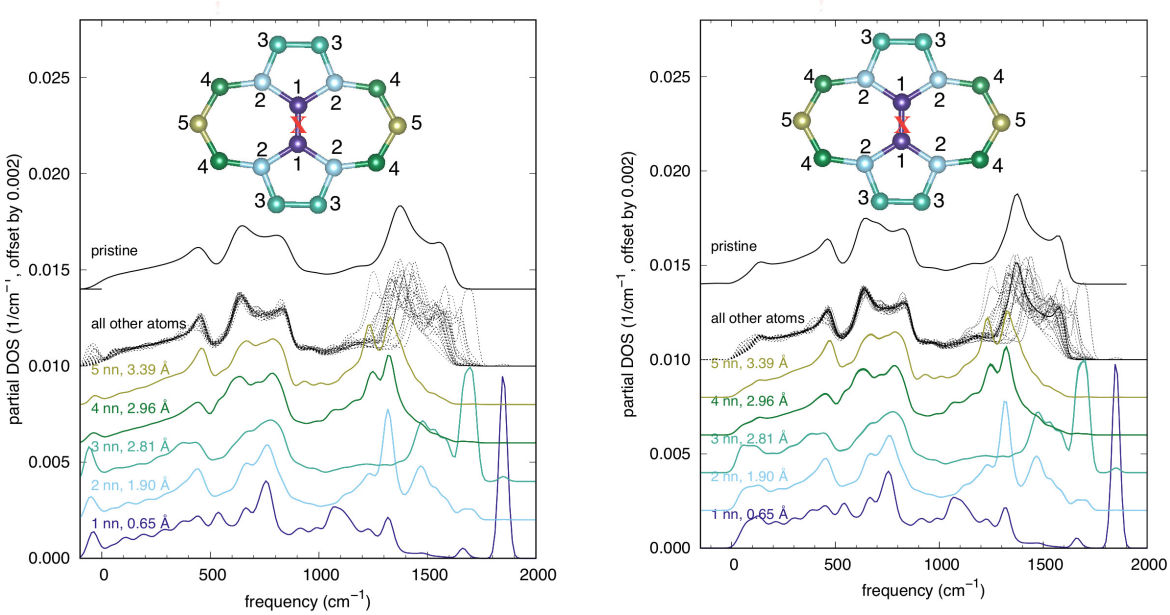

Fig. 10 Partial phonon DOS of atoms near the Dienes defect in graphene (left) and graphite (right), where nn denotes nearest neighbor and the distances are given relative to the center of the rotated C-C bond, denoted by the red "X". Atoms beyond 5 nn are plotted together (all other atoms), and the partial phonon DOS of an atom from the pristine material (pristine) is also shown. All phonon DOS plots are offset by 0.002 1/cm^{-1} for clarity. A mesh of 10 $\times$ 10 $\times$ 8 was used to generate the projected DOS.

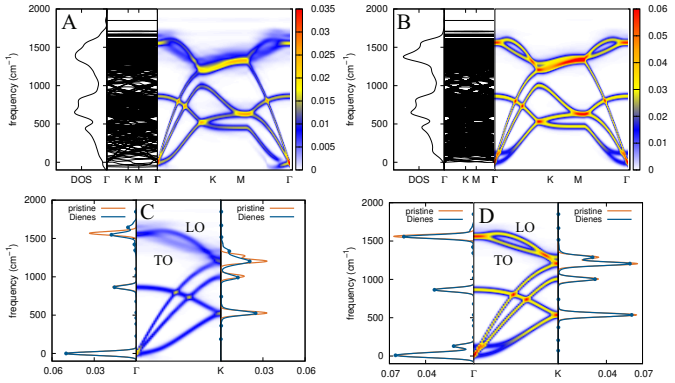

Fig. 11 Phonon DOS, folded, and unfolded band structures of Dienes-defective graphene (A) and graphite (B). (C) and (D) show line cuts of the spectral weight at the Γ and K points of Dienes-defective graphene (C) and graphite (D) where points denote maxima in the spectral weight of the defective system.

gies for the two types of defects in graphene were on the same order ∼0.1 eV, but the shifts in graphite differed by an order of magnitude (0.05 eV for the monovacancy and 0.004 eV for the Dienes defect). Additionally, the direction of change was different. The monovacancy defect lowered E_F, and the Dienes defect increased it. Both defects introduced flat bands at the Γ point, near +0.2 and +0.5 eV for the monovacancy and Dienes defects, respectively. This phenomena has been reported by others and is not unique to monovacancy and Dienes defects.[71,72] In fact, Feng et al. measured flat bands near E_F for graphene grain boundaries using scanning tunneling spectroscopy.[73]

Structural relaxations in response to the Dienes defect are more long range than the monovacancy, which partially occurs because of the size and shape of the defects. The monovacancy defect forms a pentagon and distorted nonagon, but neither the length nor width of the defect exceeds 5 Å. The Dienes defect forms a pair of pentagons and a pair of heptagons 5.4 and 6.8 Å, respectively, at the widest points. Thus, the Dienes defect has larger spatial extent in the system than the monovacancy. The difference in size leads to more atoms that are nearest neighbors to the defect. This is evidenced by more closely comparing the distance of nearest neighbors from the defect (missing atom in the monovacancy and center of the rotated C–C bond in the Dienes defect) reported in Figures 5 and 10. For the Dienes defect, a third nearest neighbor is found 2.81 Å away from the defect, and the sixth nearest neighbor in the monovacancy is found at nearly the same distance (2.82 Å). The symmetry of the defects is also quite different. Although the monovacancy defect has two-fold in-plane symmetry with a mirror plane bisecting the structure through the atom that displaces out-of-plane, the Dienes defect has four-fold in-plane symmetry with mirror planes that run through the rotated C–C bond at 0° and 90°.

The Dienes defect causes a larger change in the phonons of graphitic materials than the monovacancy defect. Although the high-frequency phonons of monovacancy-defective graphene showed slight changes in the density and frequency of peaks above 1000 cm^{-1}, these changes were small compared to the significant broadening seen for the Dienes defect, which removes the resolution of the three highest-frequency Van Hove singularities. Additionally, the Dienes defect leads to new phonons above 1700 cm^{-1}, well above the highest frequency modes in the pristine or monovacancy-defective systems, which can serve as an indicator of the Dienes defect.

One of the workhorse methods for experimentally investigating

the phonons of CF materials is Raman spectroscopy. The Raman spectra of all graphitic materials contains a peak near 1580 cm^{-1}, which arises from the in-plane bond-stretching of sp^2 carbons causing a subtle shearing of the graphitic layers with E_{2g} symmetry at the Γ point.[68,69,74] We find a band near this frequency in all systems and confirm the eigenvectors are consistent with the E_{2g} mode. Thus, we can conclude our modes at 1558 in pristine graphene and graphite are the *G* peak from Raman spectroscopy. We see minor shifts in frequency of the *G* band in the presence of defects. In graphene, the monovacancy redshifts this mode by 11 cm^{-1}, and the Dienes defect redshifts it by 4 cm^{-1}. Additionally, the mode is broadened by the Dienes defect, and we would expect the Raman-measured peak to widen when this defect is present.

Raman spectra of defective graphitic materials also contain a peak near 1350 cm^{-1} for laser excitation of 514 nm, which is highly dispersive with excitation energy. This peak is believed to arise from an intervalley double resonance process of A_{1g} symmetry at the K point and is called the *D* peak.[75–77] In our calculations, we find three modes in graphene and two in graphite with eigenvectors that resemble those of the A_{1g} breathing mode of the *D* peak (ESI†, Figs. 11 and 12). The first is at 1202 and 1203 cm^{-1} in pristine graphene and graphite, respectively. Only small shifts in frequency are seen for this mode in the defective systems (less than 10 cm^{-1}). The second mode that may contribute to the experimental *D* peak is at 1274 and 1289 cm^{-1} in pristine graphene and graphite, respectively. The Dienes defect in graphene shifts this peak to 1282 cm^{-1}, but the monovacancy defect and Dienes defect in graphite show minimal changes to the mode's frequency (less than 3 cm^{-1}).

4 Conclusions

In conclusion, we have calculated the electronic structure and phonons of monovacancy- and Dienes-defective graphene and graphite systems using DFT. From this, we calculated the formation energy, electron and phonon band structure, and electron and phonon DOS of the pristine and defective systems to determine indicators of the defects. In general, we showed that monovacancy defects open an electronic bandgap at K for defect densities greater than 1%, but no gap is opened at the same density of Dienes defects. Both defects, however, created flat electronic bands near the Fermi energy at Γ. The DOS for monovacancy defects is slightly reduced above 1300 cm^{-1} while new phonons at K in the BZ are formed. For Dienes defects, the density of modes above 1000 cm^{-1} are significantly reduced. Also note the highest frequency optical modes are significantly softened and new modes, characteristic of the rotated C–C bond vibration, are formed near 1850 cm^{-1}, which may serve as a spectral indicators of Dienes defects. Additionally, we identified several modes in the region of 1200–1350 cm^{-1} that could contribute to the experimentally observed *D* peak in the Raman spectra and noted a large redshift is peak frequency in Dienes-defect graphene.

Conflicts of interest

There are no conflicts to declare.

Acknowledgements

This research used resources of the Oak Ridge Leadership Computing Facility, which is a US Department of Energy, Office of Science User Facility supported under Contract no. DE-AC05-00OR22725. This research also used resources of the Compute and Data Environment for Science (CADES) at Oak Ridge National Laboratory, which is supported by the US Department of Energy, Office of Science under Contract no. DE-AC05-00OR22725.

The authors would also like to thank the developers of RMG for user assistance and access their RMG-Phonopy interface.

Notes and references

1 S. B. Shea, *54.5 MPG and Beyond: Materials Lighten the Load for Fuel Economy*, 2012, https://www.energy.gov/articles/545-mpg-and-beyond-materials-lighten-load-fuel-economy.

2 Ford Motor Company, *Carbon Fiber Technology that Could Deliver More Fuel-Efficient Vehicles*, 2012, https://phys.org/news/2012-10-carbon-fiber-technology-fuel-efficient-vehicles.html.

3 *Department of Energy Announces $33 Million in Funding for Carbon Neutral Hybrid Electric Aviation*, 2020, https://www.energy.gov/articles/department-energy-announces-33-million-funding-carbon-neutral-hybrid-electric-aviation.

4 B. A. Newcomb, *Composites Part A: Applied Science and Manufacturing*, 2016, **91**, 262–282.

5 R. Böhm, M. Thieme, D. Wohlfahrt, D. S. Wolz, B. Richter and H. Jäger, *Fibers*, 2018, **6**, 56.

6 X. Huang, *Materials*, 2009, **2**, 2369–2403.

7 M. D. Jiao, L. Wang, C. Y. Wang, Q. Zhang, S. Y. Ye and F. Y. Wang, *Physics Letters A*, 2016, **380**, 609–613.

8 C. Kim, S. H. Park, J. I. Cho, D. Y. Lee, T. J. Park, W. J. Lee and K. S. Yang, *Journal of Raman Spectroscopy*, 2004, **35**, 928–933.

9 H. Okuda, R. J. Young, D. Wolverson, F. Tanaka, G. Yamamoto and T. Okabe, *Carbon*, 2018, **130**, 178–184.

10 L. M. Malard, M. A. Pimenta, G. Dresselhaus and M. S. Dresselhaus, *Physics Reports*, 2009, **473**, 51–87.

11 E. A. Morris, M. C. Weisenberger, M. G. Abdallah, F. Vautard, H. Grappe, S. Ozcan, F. L. Paulauskas, C. Eberle, D. Jackson, S. J. Mecham and A. K. Naskar, *Carbon*, 2016, **101**, 245–252.

12 F. Vautard, J. Dentzer, M. Nardin, J. Schultz and B. Defoort, *Applied Surface Science*, 2014, **322**, 185–193.

13 J. L. Niedziela, A. J. Miskowiec, J. J. Langford and R. J. Kapsimalis, Proceedings of Carbon 2019, Lexington, KY, 2019, pp. 5–7.

14 A. Sadezky, H. Muckenhuber, H. Grothe, R. Niessner and U. Pöschl, *Carbon*, 2005, **43**, 1731–1742.

15 O. Frank, G. Tsoukleri, I. Riaz, K. Papagelis, J. Parthenios, A. C. Ferrari, A. K. Geim, K. S. Novoselov and C. Galiotis, *Nature Communications*, 2011, **2**, 255.

16 Z. Brubaker, R. J. Kapsimalis and J. L. Niedziela, *accepted*.

17 P. Gutmann, J. Moosburger-Will, S. Kurt, Y. Xu and S. Horn, *Polymer Degradation and Stability*, 2019, **163**, 174–184.

18 T. H. Liu, G. Gajewski, C. W. Pao and C. C. Chang, *Carbon*, 2011, **49**, 2306–2317.

19 R. H. Telling, C. P. Ewels, A. A. El-Barbary and M. I. Heggie, *Nature Materials*, 2003, **2**, 333–337.

20 L. Li, S. Reich and J. Robertson, *Physical Review B*, 2005, **72**, 184109.

21 S. B. Isbill, A. E. Shields, D. J. Mattei-Lopez, R. J. Kapsimalis and J. L. Niedziela, *Computational Materials Science*, 2021, **195C**, 110477.

22 D. H. Kim, M. S. Kim and H. D. Kim, *Applied Surface Science*, 2015, **359**, 55–60.

23 Y. Zhou, K. Jolley, R. Phillips, R. Smith and H. Wu, *Carbon*, 2019, **154**, 192–202.

24 R. Faccio and A. W. Mombrú, *Journal of Physics Condensed Matter*, 2012, **24**, 375304.

25 S. N. Shirodkar and U. V. Waghmare, *Physical Review B*, 2012, **86**, 165401.

26 S. Kida, M. Yamamoto, K. Tada, H. Kawata, Y. Hirai and M. Yasuda, *Journal of Vacuum Science & Technology A*, 2015, **33**, 05E127.

27 V. N. Popov, L. Henrard and P. Lambin, *Carbon*, 2009, **47**, 2448–2455.

28 K. Yamashita, M. Saito and T. Oda, *Japanese Journal of Applied Physics*, 2006, **45**, 6534–6536.

29 P. A. Denis, R. Faccio and F. Iribarne, *Computational and Theoretical Chemistry*, 2012, **995**, 1–7.

30 J. D. Wadey, A. Markevich, A. Robertson, J. Warner, A. Kirkland and E. Besley, *Chemical Physics Letters*, 2016, **648**, 161–165.

31 G.-D. Lee, C. Z. Wang, E. Yoon, N. M. Hwang, D. Y. Kim and K. M. Ho, *Physical Review Letters*, 2005, **95**, 205501.

32 A. S. Fedorov, D. A. Fedorov, Z. I. Popov, Y. E. Anan'eva, N. S. Eliseeva and A. A. Kuzubov, *Journal of Experimental and Theoretical Physics*, 2011, **112**, 820–824.

33 R. Babar and M. Kabir, *Physical Review B*, 2018, **98**, 075439.

34 C. D. Latham, M. I. Heggie, M. Alatalo, S. Öberg and P. R. Briddon, *Journal of Physics Condensed Matter*, 2013, **25**, 135403.

35 M. C. Wang, C. Yan, L. Ma, N. Hu and M. W. Chen, *Computational Materials Science*, 2012, **54**, 236–239.

36 M. M. Ugeda, I. Brihuega, F. Guinea and J. M. Gómez-Rodríguez, *Physical Review Letters*, 2010, **104**, 096804.

37 Y. Ma, P. O. Lehtinen, A. S. Foster and R. M. Nieminen, *New Journal of Physics*, 2004, **6**, 68.

38 E. Nakhmedov, E. Nadimi, S. Vedaei, O. Alekperov, F. Tatardar, A. I. Najafov, I. I. Abbasov and A. M. Saletsky, *Physical Review B*, 2019, **99**, 125125.

39 A. Weerasinghe, A. Ramasubramaniam and D. Maroudas, *Materials Research Express*, 2018, **5**, 115603.

40 O. V. Yazyev, *Reports on Progress in Physics*, 2010, **73**, 056501.

41 A. M. Valencia and M. J. Caldas, *Physical Review B*, 2017, **96**, 125431.

42 P. O. Lehtinen, A. S. Foster, Y. Ma, A. V. Krasheninnikov and R. M. Nieminen, *Physical Review Letters*, 2004, **93**, 187202.

43 S. Li and Z. T. Lv, *Chinese Physics B*, 2017, **26**, 036303.

44 J. Ma, D. Alfè, A. Michaelides and E. Wang, *Physical Review B*, 2009, **80**, 033407.

45 J. R. Yin, W. H. Wu, W. Xie, Y. H. Ding and P. Zhang, *Physica E: Low-Dimensional Systems and Nanostructures*, 2015, **68**, 102–106.

46 S. Chowdhury, S. Baidya, D. Nafday, S. Halder, M. Kabir, B. Sanyal, T. Saha-Dasgupta, D. Jana and A. Mookerjee, *Physica E: Low-Dimensional Systems and Nanostructures*, 2014, **61**, 191–197.

47 I. Al-Qasir, A. A. Campbell, G. Sala, J. Y. Y. Lin, Y. Cheng, F. F. Islam, D. Abernathy and M. B. Stone, *Carbon*, 2020, **168**, 42–54.

48 M. Mohr, J. Maultzsch, E. Dobardžić, S. Reich, I. Milošević, M. Damnjanović, A. Bosak, M. Krisch and C. Thomsen, *Physical Review B*, 2007, **76**, 035439.

49 G. Bouzerar, S. Thébaud, S. Pecorario and C. Adessi, *J. Phys.: Condens. Matter*, 2020, **32**, 295702.

50 E. Briggs, D. Sullivan and J. Bernholc, *Physical Review B*, 1996, **54**, 14362–14375.

51 M. Hodak, S. Wang, W. Lu and J. Bernholc, *Physical Review B*, 2007, **76**, 085108.

52 J. Zhang, Y. Cheng, W. Lu, E. Briggs, A. J. Ramirez-Cuesta and J. Bernholc, *Journal of Chemical Theory and Computation*, 2019, **15**, 6859–6864.

53 M. Dion, H. Rydberg, E. Schröder, D. C. Langreth and B. I. Lundqvist, *Physical Review Letters*, 2004, **92**, 246401.

54 K. F. Garrity, J. W. Bennett, K. M. Rabe and D. Vanderbilt, *Computational Materials Science*, 2014, **81**, 446–452.

55 M. Methfessel and A. T. Paxton, *Physical Review B*, 1989, **40**, 3616–3621.

56 L. Chaput, A. Togo, I. Tanaka and G. Hug, *Physical Review B*, 2011, **84**, 094302.

57 A. Togo, L. Chaput and I. Tanaka, *Physical Review B*, 2015, **91**, 094306.

58 A. M. Ganose, A. J. Jackson and D. O. Scanlon, *Journal of Open Source Software*, 2018, **3**, 717.

59 Y. Hinuma, G. Pizzi, Y. Kumagai, F. Oba and I. Tanaka, *Computational Materials Science*, 2017, **128**, 140–184.

60 A. Togo and I. Tanaka, *Spglib: A Software Library for Crystal Symmetry Search*, 2018.

61 M. Farjam, *Journal of Physics Condensed Matter*, 2014, **26**, 155502.

62 Y. Ikeda, A. Carreras, A. Seko, A. Togo and I. Tanaka, *Physical Review B*, 2017, **95**, 024305.

63 A. A. El-Barbary, R. H. Telling, C. P. Ewels, M. I. Heggie and P. R. Briddon, *Physical Review B*, 2003, **68**, 144107.

64 M. G. Menezes and R. B. Capaz, *Journal of Physics Condensed Matter*, 2015, **27**, 335302.

65 A. Pisanty, *Journal of Chemical Education*, 1991, **68**, 804–808.

66 G. Yang, L. Li, W. B. Lee and M. C. Ng, *Science and Technology*

of Advanced Materials, 2018, **19**, 613–648.

67 S. Piscanec, M. Lazzeri, F. Mauri, A. C. Ferrari and J. Robertson, *Physical Review Letters*, 2004, **93**, 185503.

68 F. Tuinstra and J. L. Koenig, *The Journal of Chemical Physics*, 1970, **53**, 1126–1130.

69 A. C. Ferrari, *Solid State Communications*, 2007, **143**, 47–57.

70 A. I. Podlivaev and L. A. Openov, *JETP Letters*, 2015, **101**, 173–176.

71 N. M. Peres, F. Guinea and A. H. Castro Neto, *Physical Review B*, 2006, **73**, 125411.

72 M. M. Ugeda, D. Fernández-Torre, I. Brihuega, P. Pou, A. J. Martínez-Galera, R. Pérez and J. M. Gómez-Rodríguez, *Physical Review Letters*, 2011, **107**, 116803.

73 L. Feng, X. Lin, L. Meng, J. C. Nie, J. Ni and L. He, *Applied Physics Letters*, 2012, **101**, 113113.

74 M. R. Ammar, N. Galy, J. N. Rouzaud, N. Toulhoat, C. E. Vaudey, P. Simon and N. Moncoffre, *Carbon*, 2015, **95**, 364–373.

75 M. J. Matthews, M. A. Pimenta, G. Dresselhaus, M. S. Dresselhaus and M. Endo, *Physical Review B*, 1999, **59**, R6585–R6588.

76 C. Thomsen and S. Reich, *Physical Review Letters*, 2000, **85**, 5214–5217.

77 R. Saito, A. Jorio, A. G. Souza Filho, G. Dresselhaus, M. S. Dresselhaus and M. A. Pimenta, *Physical Review Letters*, 2002, **88**, 027401.